nature physics

LETTERS

PUBLISHED ONLINE: 11 MAY 2015 | DOI: 10.1038/NPHYS3324

# Observation of biexcitons in monolayer $WSe_2$

Yumeng You[1,2†], Xiao-Xiao Zhang[2†], Timothy C. Berkelbach[3], Mark S. Hybertsen[4], David R. Reichman[3] and Tony F. Heinz[2*‡]

**Transition metal dichalcogenide (TMDC) crystals exhibit new emergent properties at monolayer thickness[1,2], notably strong many-body effects mediated by Coulomb interactions[3–6]. A manifestation of these many-body interactions is the formation of excitons, bound electron–hole pairs, but higher-order excitonic states are also possible. Here we demonstrate the existence of four-body, biexciton states in monolayer $WSe_2$. The biexciton is identified as a sharply defined state in photoluminescence at high exciton density. Its binding energy of 52 meV is more than an order of magnitude greater than that found in conventional quantum-well structures[7]. A variational calculation of the biexciton state reveals that the high binding energy arises not only from strong carrier confinement, but also from reduced and non-local dielectric screening. These results open the way for the creation of new correlated excitonic states linking the degenerate valleys in TMDC crystals, as well as more complex many-body states such as exciton condensates or the recently reported dropletons[8].**

TMDC crystals, including $MoS_2$, $MoSe_2$, $WS_2$ and $WSe_2$, are semiconductors that form layered structures with a plane of hexagonal metal atoms surrounded by two planes of chalcogen atoms in trigonal prismatic coordination. At monolayer thickness, these crystals exhibit direct band gaps at the K and K′ points in the Brillouin zone[1,2], and recent studies have revealed the possibility of selectively accessing the K or K′ valley through the use of circularly polarized light[9–12], as well as the existence of an associated valley Hall effect[13]. Importantly, many-body Coulomb interactions in these monolayer TMDC crystals have been found to be particularly strong. This leads to excitonic optical transitions in the materials, with exciton binding energies of several hundred meV (refs 3–6). In the presence of free charges, stable charged excitons (trions) have also been identified and exhibit binding energies of tens of meV (refs 12,14–16).

In view of the prominence of these two- and three-body excitonic states, it is natural to ask whether two-dimensional (2D) TMDC materials, just as for the much-studied zero- and one-dimensional nanostructures[7,17–21], also support the formation of stable biexcitons[22,23]. Here we demonstrate the presence of biexcitons in monolayer $WSe_2$ through the discovery of a sharp new emission peak under pulsed laser excitation. We further probe the properties of the biexciton state through measurements of its ultrafast dynamics, valley polarization and thermal stability. We establish a biexciton binding energy of 52 meV. This unusually high binding energy is compatible with results of a variational analysis of biexcitonic states performed using a non-locally screened Coulomb potential to describe the interactions of charges in the atomically thin 2D material.

To identify the biexciton states, we have studied the photoluminescence (PL) under ultrafast pump radiation at different fluences, producing different exciton densities. We compare the PL spectra for a $WSe_2$ monolayer at a temperature of 50 K for two excitation fluences (Fig. 1a). The higher applied fluence of 12 $\mu J\,cm^{-2}$ yields an exciton density up to $5 \times 10^{11}\,cm^{-2}$ (see Methods). Several distinct emission features are observed in the PL spectra, most of which have been identified in previous investigations at low excitation density[12]. In particular, the peak at 1.74 eV arises from emission from neutral excitons (X) and the peak at 1.71 eV from negative trions ($X^-$). At lower photon energies, we see additional emission features, which we label as $P_0$ to $P_3$. Features $P_1$ to $P_3$ grow more slowly than exciton emission with increasing pump fluence, exhibiting sublinear fluence dependence. We assign $P_1$ to $P_3$ to emission from bound excitons at defect sites[24], in agreement with previous PL studies[12,25].

The behaviour of peak $P_0$ at 1.68 eV is, however, different from that of the other lower-energy features. This feature grows superlinearly with fluence. To probe the properties of emission feature $P_0$ in more detail, we have measured PL spectra at 10 K over a wide range of excitation fluence (Fig. 1b). At high excitation densities, feature $P_0$ emerges as the strongest emission channel.

For a quantitative analysis of the different emission states, we fit the emission spectra to a form with one symmetrical feature for each of the $P_0$–$P_3$, X and $X^-$ peaks (see Supplementary Information). We obtain (Fig. 1b) a good representation of the observed spectra at different excitation fluences solely by varying the intensity of the emission peaks; the energies and linewidths of the features are unchanged with fluence.

Our primary interest lies in understanding the superlinear behaviour of the $P_0$ feature. To minimize the influence of defect states, we analyse emission from the $P_0$ feature in terms of the strength of the neutral exciton emission. As the emission times of X, $X^-$ and $P_0$ show no significant variation with fluence (see below), we associate the strengths of the PL features with the population of the corresponding emitting species. Figure 1c shows the emission strength $I_{P_0}$ of the $P_0$ species as a function of the emission intensity $I_X$ of the neutral exciton. The $P_0$ data can be described adequately by a power-law relation of the form $I_{P_0} \propto {I_X}^{\alpha}$, with $\alpha = 1.39$. (See Supplementary Information for further discussion of the fluence dependence of the different species.)

On the basis of the superlinear strength of emission from the $P_0$ species with respect to X emission, we identify this feature as arising from a biexciton (XX) state. Under conditions of full thermal equilibrium (neglecting any possible rise in temperature with increased excitation fluences), we would expect a quadratic

[1]Ordered Matter Science Research Center, Southeast University, Nanjing 211189, China. [2]Departments of Physics and Electrical Engineering, Columbia University, 538 West 120th St., New York, New York 10027, USA. [3]Department of Chemistry, Columbia University, 3000 Broadway, New York, New York 10027, USA. [4]Center for Functional Nanomaterials, Brookhaven National Laboratory, Upton, New York 11973-5000, USA. †These authors contributed equally to this work. ‡Present addresses: Department of Applied Physics, Stanford University, Stanford, California 94305, USA; SLAC National Accelerator Laboratory, 2575 Sand Hill Rd., Menlo Park, California 94025, USA. *e-mail: tony.heinz@stanford.edu

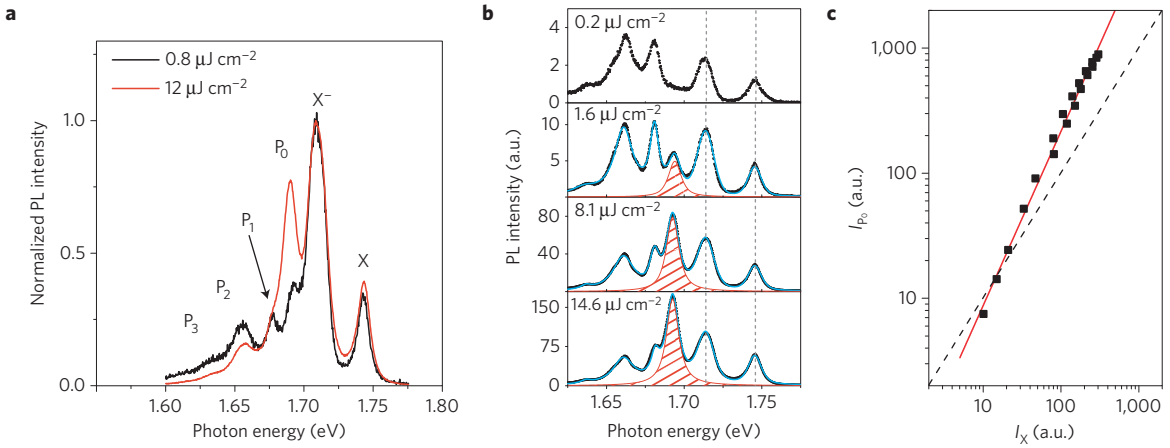


**Figure 1 | Photoluminescence spectra and intensities of monolayer $WSe_2$ for different pump fluences. a**, PL spectra at 50 K for pulsed excitation under applied fluences of 0.8 μJ cm$^{-2}$ and 12 μJ cm$^{-2}$. The spectra are normalized to yield the same emission strength for the neutral exciton. **b**, PL spectra and spectral fitting at 10 K for the indicated applied fluences. The major emission features are the same as those in **a**. The vertical grey lines show that there is no peak shift of the features with fluence. The black dots are experimental data, and the solid blue lines are based on a fit with one feature for each peak, where only the peak amplitudes are changed for the different spectra. The component of the $P_0$ peak is shown separately in red. **c**, Logarithmic plot of the $P_0$ emission strength, $I_{P_0}$, as a function of the exciton emission strength $I_X$. The red line is a power-law fit: $I_{P_0} \propto I_X^{\alpha}$, with $\alpha = 1.39$. For comparison, a linear relation is shown as a dashed black line.

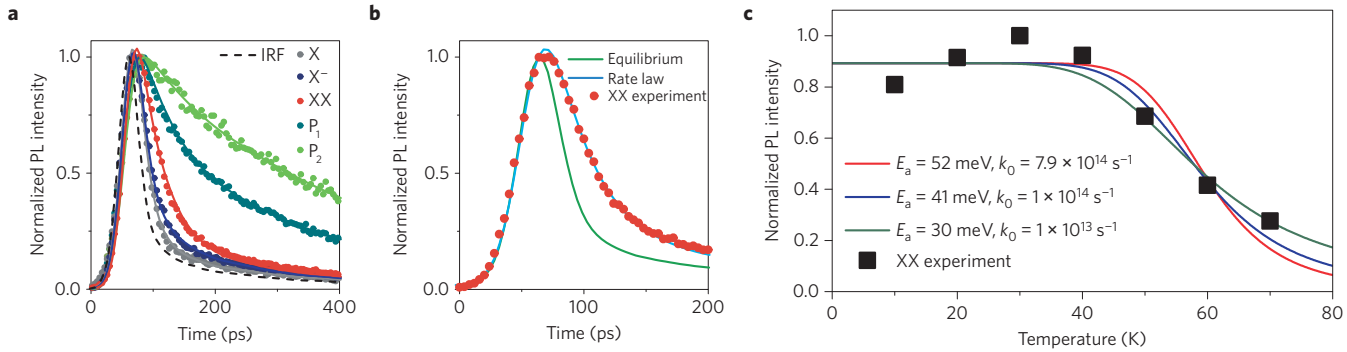


**Figure 2 | Dynamics and thermal stability of excited states. a**, Time-resolved PL traces for X, $X^-$, XX, $P_1$ and $P_2$ species (dots, with solid lines as guides to the eye) and the instrument response function (IRF). The two defect-related peaks, $P_1$ and $P_2$, have decay times >100 ps, whereas the X, $X^-$ and XX features decay rapidly. Based on a single exponential fit, the emission lifetimes are $\tau_X = 14$ ps, $\tau_{X^-} = 25$ ps and $\tau_{XX} = 31$ ps, with uncertainties of ±5 ps. **b**, Experimental TR-PL for the biexciton species compared with the expected behaviour based on the measured exciton dynamics. The green line is a fit based on an equilibrium model with a quadratic relation between the biexciton and exciton populations. The blue line is based on the rate equation described in the text. **c**, The squares show the relative PL emission measured from the biexciton state as a function of sample temperature for an applied laser fluence of 0.8 μJ cm$^{-2}$. The solid curves are predicted emission strengths based on the thermal dissociation model described in the text for the indicated activation energies $E_a$ and pre-factors $k_0$.

relation between the density of biexcitons and excitons[17]—that is, $I_{XX} \propto I_X^{\alpha}$ with $\alpha = 2$. However, in quantum-well systems, for which biexcitons have been extensively studied[7], exponents of $\alpha = 1.2$–$1.9$ are typically observed, and attributed to the lack of equilibrium between the states[18,26]. The strong biexciton emission compared to exciton emission that we observe has previously been reported in quantum-well systems at low temperatures and elevated excitation densities[27].

To further examine the biexciton state, we have investigated its dynamics using time-resolved PL (TR-PL). In Fig. 2a, we compare TR-PL traces for XX emission with those from the excitonic states (X, $X^-$) and from the strongest defect species ($P_1$, $P_2$). All of the time traces can be fitted to a rapid rise, comparable to the instrumental response, but the decay times differ strongly. The lifetimes of the exciton, trion and biexciton states are tens of picoseconds, whereas the emission lifetime for $P_1$ and $P_2$ defect features exceeds 100 ps. This result provides further evidence for the validity of the assignment of the $P_0$ emission as arising from biexcitons, rather than from any type of defect state. The short emission times of X, $X^-$ and XX features are compatible with the lack of full thermal equilibrium between the exciton and biexciton, as mentioned above. The emission times of the exciton and biexciton states were investigated as a function of the pump fluence. No appreciable variation in the emission time with fluence was observed. The result indicates that depletion of excitons by an exciton–exciton annihilation process[28,29] is not significant under our experimental conditions.

We can use the inferred single exciton dynamics to predict the biexciton dynamics and compare with the observed biexciton TR-PL. Under the assumption of full thermal equilibrium, the biexciton density $N_{XX}$ will vary quadratically with the exciton density $N_X$ at all times[17]. From the measured dynamics for $N_X$, we then predict the TR-PL for biexciton emission (Fig. 2b), which clearly does not match experimental results. On the other hand, the measured biexciton

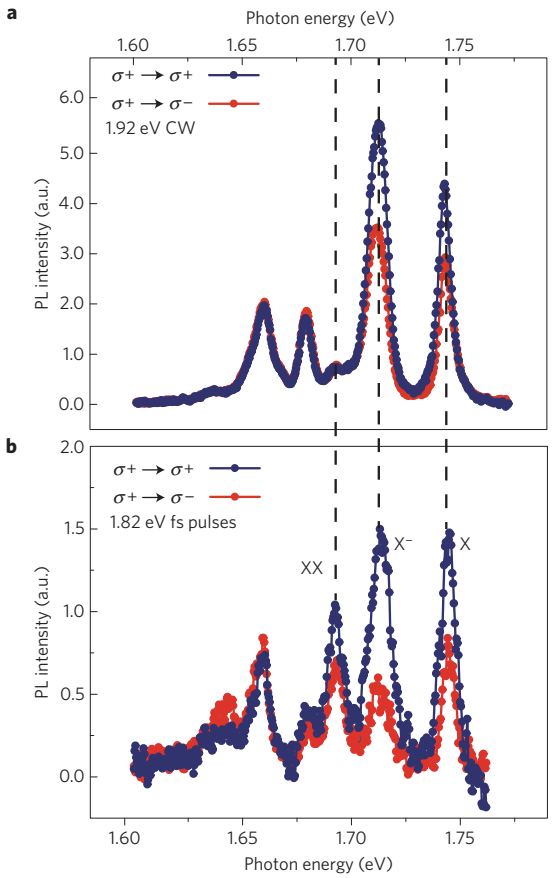


**Figure 3 | Analysis of circularly polarized emission components for excitation by near-resonant circularly polarized radiation. a**,**b**, PL spectra for the same (blue) and opposite (red) circularly polarized states for the $WSe_2$ monolayer at 15 K. The emission energies for neutral (X) and charged ($X^-$) excitons and the biexciton (XX) state are indicated by dashed lines. **a**, Results for low exciton density with CW excitation at a photon energy of 1.92 eV. Defining the degree of circular polarization as $\rho = [I(\sigma^+) - I(\sigma^-)]/[I(\sigma^+) + I(\sigma^-)]$, where $\sigma^\pm$ denotes the polarization state detected for $\sigma^+$ excitation, we obtain $\rho(X) = 0.20$ and $\rho(X^-) = 0.38$, whereas $|\rho| < 0.05$ for the defect states. **b**, Results for high exciton density with pulsed excitation at a photon energy of 1.82 eV. The biexciton feature is now present in the PL spectra and exhibits significant circular polarization, with $\rho(XX) = 0.16$. The other features show similar behaviour as for the case of low excitation density, with $\rho(X) = 0.30$ and $\rho(X^-) = 0.50$, whereas $|\rho| < 0.05$ for the defect states.

TR-PL is compatible with predictions (Fig. 2b) of a non-thermalized model based on a simple rate-equation:

$$\frac{dN_{XX}}{dt} = \beta N_X^2 - \gamma N_{XX} \quad (1)$$

Here $\beta = 1.1\ cm^2\ s^{-1}$ represents the biexciton formation rate from collisions of excitons, where we have assumed in the analysis that each absorbed photon initially produces an exciton. Using kinetic theory for thermalized excitons, we infer from $\beta$ (Methods) a cross-section for biexciton formation of ~4 nm, comparable to the exciton Bohr radius[30]. Our fitting procedure yields a biexciton relaxation time of $\gamma^{-1} = 27$ ps, which is attributed primarily to non-radiative decay channels. The biexciton dissociation process is suppressed at low temperatures, as discussed below. This effectively decouples the exciton and biexciton dynamics, permitting a longer lifetime for biexcitons than for excitons. A similar experimental finding of

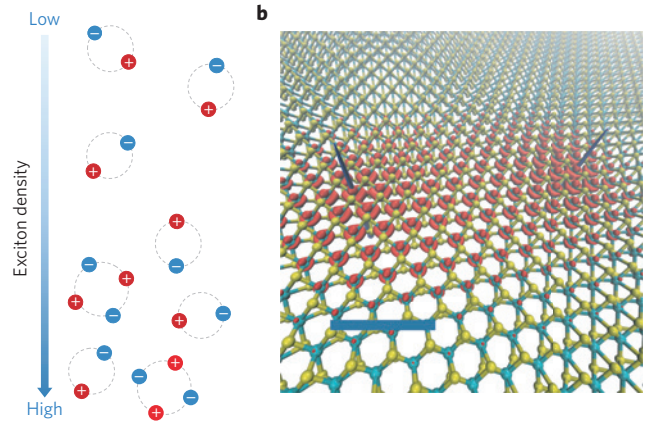


**Figure 4 | Real-space representation of biexcitons. a**, Schematic representation of biexcitons as four-body quasiparticles. With increasing exciton density biexcitons are formed from excitons. **b**, Real-space representation of the biexciton projected onto the $WSe_2$ plane as determined by the variational calculation described in the text. The red regions indicate distribution of the total charge of the two electrons in the biexciton when the two holes (blue peaks) are fixed at a typical separation of 3.3 nm. The scale bar is 1 nm.

longer biexciton than exciton lifetimes has been previously reported in the literature for (Zn, Cd)Se/ZnSe quantum wells[27].

The nature of biexcitonic states and the valley occupancy of these states can be probed through investigation of the polarization characteristics of the photoluminescence. To this end, we used near-resonant circularly polarized excitation (Methods) to produce excitons preferentially in one valley (K or K′; refs 9–12). For low exciton density under continuous wave (CW) laser excitation, the X, $X^-$ and defect-related emission peaks are observed (Fig. 3a); at high exciton density produced by pulsed laser excitation, we also observe XX emission (Fig. 3b). The peaks for X, $X^-$ and XX (under pulsed excitation) all exhibit significant circular polarization. The two major defect-related emission peaks, on the other hand, show no measurable circular polarization character. This result provides additional evidence that defects do not play a role in the peak identified as the biexciton.

The polarization of the biexciton emission also reflects the valley character of this many-body state. Exchange and correlation effects could induce differences in the stability of biexcitons formed from two excitons in the same valley or in opposite valleys. For near-resonant excitation with circularly polarized light, we observe biexciton emission with both the same and opposite circularly polarized state (Fig. 3b). We expect the former to arise more strongly from intravalley excitons than the latter. The biexciton emission spectra for these two cases, as well as for linearly polarized excitation and excitation with higher photon energy, are indistinguishable. The measurements thus suggest that both intra- and intervalley biexcitons can be formed and that they exhibit the same emission energies (within 1 meV).

Taken together, the observed fluence dependence, temporal dynamics and circular polarization properties of the $P_0$ feature provide strong evidence for its assignment as a biexciton feature. We now consider experimental observations related to the biexciton binding energy and thermal stability.

The biexciton binding energy is defined as the difference in energy between two free excitons and the biexciton state: $\Delta_{XX} = 2E_X - E_{XX}$. We determine $E_{XX}$ through observation of the biexciton photoluminescence at energy $\hbar\omega_{XX}$ and information about the remaining excitation in the material. If we assume that radiative decay of the biexciton produces an exciton, then

$E_{XX} = \hbar\omega_{XX} + E_X = \hbar\omega_{XX} + \hbar\omega_X$, where $\hbar\omega_X$ denotes the exciton emission energy. Thus, the biexciton binding energy is given by the spectral shift: $\Delta_{XX} = \hbar\omega_X - \hbar\omega_{XX} = 52$ meV. We note that in this system there are other types of excitons—namely, trions and dark excitons[31]. We discuss the possible influence of these species in the Supplementary Information. We also present experimental data on the change in emission energies and intensities induced by different dielectric environments and charge densities of the sample.

We investigated the stability of the biexciton using temperature-dependent PL measurements. Under the same excitation condition, the biexciton emission intensity shows a plateau at low temperature, but decreases significantly for temperature $T > 70$ K (Fig. 2c). This trend can be explained by a model in which biexcitons have a roughly constant rate of formation as a function of $T$, but exhibit a thermally activated dissociation channel, corresponding to a decay rate in equation (1) of the form $\gamma(T) = {\tau_{XX}}^{-1} + k_0 \exp(-E_a/k_B T)$. The observed temperature dependence is compatible with activation energies $E_a$ from 30 to 50 meV (see Fig. 2c and Supplementary Section 7).

It is instructive to compare the biexciton binding energy in $WSe_2$ monolayers with those of conventional quasi-2D structures. The value of $\Delta_{XX} = 52$ meV for the former exceeds that found in III–V quantum wells by almost two orders of magnitude[7]. This remarkably large $\Delta_{XX}$ must, however, be considered in light of the overall strength of the Coulomb interactions. If we normalize $\Delta_{XX}$ in $WSe_2$ to the exciton binding energy in the same system, recently reported as 370 meV (ref. 5), we obtain a ratio, the so-called Haynes factor, of 0.14. This ratio is similar to that found in quantum-well systems. The large $\Delta_{XX}$ in monolayer $WSe_2$ thus scales with the overall strength of the Coulomb interaction.

To obtain deeper physical insight into the biexciton state, we have performed quantum-mechanical calculations of these correlated four-particle states, represented schematically in Fig. 4a. Although biexciton states have been previously investigated for quasi-2D systems[32–34], the results cannot be directly applied to the TMDC monolayers because of the distinctive character of the electron–hole (e–h) interaction in these atomically thin materials. As has been discussed in the recent theoretical literature[30,35] and revealed in the spectrum of the excited exciton states[3–5], the strongly inhomogeneous dielectric environment gives rise to a non-local screening effect for the e–h interaction potential: the screening is strong at short range, but weak at long range. Using a biexciton Hamiltonian with such an e–h interaction potential, we have carried out a variational calculation that yields a biexciton binding energy of 37 meV for $WSe_2$ (see Methods and Supplementary Section 8). On the basis of a comparison with existing numerically exact results for a conventional screened Coulomb potential[36], we expect that the true biexciton binding energy should exceed our variational bound by an additional 40–50%. This yields a predicted $\Delta_{XX} \sim 50$–$60$ meV, in good agreement with experiment.

The nature of the biexciton states in $WSe_2$ monolayers is elucidated by examining the real-space structure of the biexciton complex predicted by our variational calculation. The biexciton consists of two distinct excitons, each with a Bohr radius equal to that of a single exciton (1 nm), separated by a distance three to four times larger (Fig. 4b). Given the large separation between charges, the screening of the Coulomb interaction will be strongly influenced by that of the external media, rather than the intrinsic screening of the $WSe_2$ monolayer. We thus expect the biexciton states to be particularly sensitive to the nature of the surrounding media.

The results presented here demonstrate that under appropriate conditions the strongest channel for light emission can occur through a biexciton channel. The prominence of such four-body correlated states in the material reflects the unusual strength of many-body interactions in atomically thin TMDC semiconductors. Monolayer TMDC materials are thus very favourable candidates for other many-body processes, such as multiple-exciton generation[37], and for the creation of new higher-order correlated states, such as exciton condensates or the recently introduced dropletons[8]. The existence of the degenerate K and K′ valleys also offers the possibility of creating optically bright biexciton states with pairs of carriers in distinct valleys. This not only induces new types of quantum coherent excitation within the solid, but also offers the possibility of the creation, through cascaded emission, of correlated photon pairs with a novel mechanism for the control of polarization states[38].

## Methods

Methods and any associated references are available in the online version of the paper.

Received 2 October 2014; accepted 24 March 2015; published online 11 May 2015

## References


1. Mak, K. F., Lee, C., Hone, J., Shan, J. & Heinz, T. F. Atomically thin MoS: A new direct-gap semiconductor. *Phys. Rev. Lett.* **105,** 136805 (2010).
2. Splendiani, A. *et al.* Emerging photoluminescence in monolayer $MoS_2$. *Nano Lett.* **10,** 1271–1275 (2010).
3. Chernikov, A. *et al.* Exciton binding energy and nonhydrogenic Rydberg series in monolayer $WS_2$. *Phys. Rev. Lett.* **113,** 076802 (2014).
4. Ye, Z. *et al.* Probing excitonic dark states in single-layer tungsten disulphide. *Nature* **513,** 214–218 (2014).
5. He, K. *et al.* Tightly bound excitons in monolayer $WSe_2$. *Phys. Rev. Lett.* **113,** 026803 (2014).
6. Ugeda, M. M. *et al.* Giant bandgap renormalization and excitonic effects in a monolayer transition metal dichalcogenide semiconductor. *Nature Mater.* **13,** 1091–1095 (2014).
7. Klingshirn, C. F. *Semiconductor Optics* Vol. 3 (Springer, 2007).
8. Almand-Hunter, A. E. *et al.* Quantum droplets of electrons and holes. *Nature* **506,** 471–475 (2014).
9. Mak, K. F., He, K., Shan, J. & Heinz, T. F. Control of valley polarization in monolayer $MoS_2$ by optical helicity. *Nature Nanotech.* **7,** 494–498 (2012).
10. Zeng, H., Dai, J., Yao, W., Xiao, D. & Cui, X. Valley polarization in $MoS_2$ monolayers by optical pumping. *Nature Nanotech.* **7,** 490–493 (2012).
11. Cao, T. *et al.* Valley-selective circular dichroism of monolayer molybdenum disulphide. *Nature Commun.* **3,** 887 (2012).
12. Jones, A. M. *et al.* Optical generation of excitonic valley coherence in monolayer $WSe_2$. *Nature Nanotech.* **8,** 634–638 (2013).
13. Mak, K. F., McGill, K. L., Park, J. & McEuen, P. L. Valleytronics. The valley Hall effect in MoS(2) transistors. *Science* **344,** 1489–1492 (2014).
14. Mak, K. F. *et al.* Tightly bound trions in monolayer $MoS_2$. *Nature Mater.* **12,** 207–211 (2013).
15. Ross, J. S. *et al.* Electrical control of neutral and charged excitons in a monolayer semiconductor. *Nature Commun.* **4,** 1474 (2013).
16. Mitioglu, A. *et al.* Optical manipulation of the exciton charge state in single-layer tungsten disulfide. *Phys. Rev. B* **88,** 245403 (2013).
17. Kim, J., Wake, D. & Wolfe, J. Thermodynamics of biexcitons in a GaAs quantum well. *Phys. Rev. B* **50,** 15099–15107 (1994).
18. Phillips, R., Lovering, D., Denton, G. & Smith, G. Biexciton creation and recombination in a GaAs quantum well. *Phys. Rev. B* **45,** 4308–4311 (1992).
19. Colombier, L. *et al.* Detection of a biexciton in semiconducting carbon nanotubes using nonlinear optical spectroscopy. *Phys. Rev. Lett.* **109,** 197402 (2012).
20. Yuma, B. *et al.* Biexciton, single carrier, and trion generation dynamics in single-walled carbon nanotubes. *Phys. Rev. B* **87,** 205412 (2013).
21. Klimov, V. I. *Semiconductor and Metal Nanocrystals: Synthesis and Electronic and Optical Properties* (CRC Press, 2003).
22. Mai, C. *et al.* Many-body effects in valleytronics: Direct measurement of valley lifetimes in single-layer $MoS_2$. *Nano Lett.* **14,** 202–206 (2014).
23. Shang, J. *et al.* Observation of excitonic fine structure in a 2D transition-metal dichalcogenide semiconductor. *ACS Nano* **9,** 647–655 (2015).
24. Tongay, S. *et al.* Defects activated photoluminescence in two-dimensional semiconductors: Interplay between bound, charged, and free excitons. *Sci. Rep.* **3,** 02657 (2013).
25. Wang, G. *et al.* Valley dynamics probed through charged and neutral exciton emission in monolayer $WSe_2$. *Phys. Rev. B* **90,** 075413 (2014).
26. Birkedal, D., Singh, J., Lyssenko, V. G., Erland, J. & Hvam, J. M. Binding of quasi-two-dimensional biexcitons. *Phys. Rev. Lett.* **76,** 672–675 (1996).
27. Spiegel, R. *et al.* Polarization-dependent formation of biexcitons in (Zn,Cd)Se/ZnSe quantum wells. *Phys. Rev. B* **55,** 9866–9871 (1997).

28. Kumar, N. *et al.* Exciton–exciton annihilation in $MoSe_2$ monolayers. *Phys. Rev. B* **89,** 125427 (2014).
29. Sun, D. *et al.* Observation of rapid exciton–exciton annihilation in monolayer molybdenum disulfide. *Nano Lett.* **14,** 5625–5629 (2014).
30. Berkelbach, T. C., Hybertsen, M. S. & Reichman, D. R. Theory of neutral and charged excitons in monolayer transition metal dichalcogenides. *Phys. Rev. B* **88,** 045318 (2013).
31. Liu, G-B., Shan, W-Y., Yao, Y., Yao, W. & Xiao, D. Three-band tight-binding model for monolayers of group-VIB transition metal dichalcogenides. *Phys. Rev. B* **88,** 085433 (2013).
32. Kleinman, D. Binding energy of biexcitons and bound excitons in quantum wells. *Phys. Rev. B* **28,** 871–879 (1983).
33. Singh, J., Birkedal, D., Lyssenko, V. G. & Hvam, J. M. Binding energy of two-dimensional biexcitons. *Phys. Rev. B* **53,** 15909–15913 (1996).
34. Riva, C., Peeters, F. M. & Varga, K. Excitons and charged excitons in semiconductor quantum wells. *Phys. Rev. B* **61,** 13873–13881 (2000).
35. Cudazzo, P., Tokatly, I. V. & Rubio, A. Dielectric screening in two-dimensional insulators: Implications for excitonic and impurity states in graphane. *Phys. Rev. B* **84,** 085406 (2011).
36. Usukura, J., Suzuki, Y. & Varga, K. Stability of two- and three-dimensional excitonic complexes. *Phys. Rev. B* **59,** 5652–5661 (1999).
37. Choi, Y., Sim, S., Lim, S. C., Lee, Y. H. & Choi, H. Ultrafast biexciton spectroscopy in semiconductor quantum dots: Evidence for early emergence of multiple-exciton generation. *Sci. Rep.* **3,** 3206 (2013).
38. Akopian, N. *et al.* Entangled photon pairs from semiconductor quantum dots. *Phys. Rev. Lett.* **96,** 130501 (2006).


## Acknowledgements

The authors would like to acknowledge valuable discussions with A. Chernikov and T. Cao and technical assistance from Y. Rao and F. Zhang. The experimental research was supported by the National Science Foundation through grants DMR-1106172 and DMR-1122594, the Keck Foundation, and the Honda Research Institute. Support for data analysis by was provided by the AMOS program, Chemical Sciences, Geosciences, and Biosciences Division, Basic Energy Sciences, US Department of Energy under Contract No. DE-AC02-76-SFO0515 (T.F.H.). This work was carried out in part at the Center for Functional Nanomaterials, Brookhaven National Laboratory, which is supported by the US Department of Energy, Office of Basic Energy Sciences, under Contract No. DE-AC02-98CH10886 (M.S.H.).

## Author contributions

Y.Y. and X-X.Z. designed the experiment, performed the measurements, interpreted the results, and wrote the manuscript; T.C.B. performed the variational calculation under the guidance of M.S.H. and D.R.R. and contributed to writing of the manuscript; T.F.H. contributed to the interpretation of the results and writing of the manuscript.

## Additional information

Supplementary information is available in the online version of the paper. Reprints and permissions information is available online at www.nature.com/reprints. Correspondence and requests for materials should be addressed to T.F.H.

## Competing financial interests

The authors declare no competing financial interests.

## Methods

**Experimental.** Monolayer $WSe_2$ crystals were prepared by mechanical exfoliation on a Si substrate covered by an oxide layer and exhibited unintentional n-doping[12] (see Supplementary Information for further information on sample preparation and other experimental details). The samples were studied in an optical cryostat using an inverted microscope. The excitation source for the photoluminescence measurements consisted of femtosecond laser pulses with a photon energy of 3.06 eV for the fluence-dependence study and time-resolved PL. These pulses, of 100 fs duration, were produced by the frequency-doubled output of a mode-locked Ti:sapphire laser operating at 80 MHz. For circular polarization measurements, femtosecond excitation pulses with a photon energy centred at 1.82 eV and a 1 MHz repetition rate were used. We obtained these pulses by filtering the supercontinuum radiation produced by focusing an amplified mode-locked fibre laser (Impulse, Clarke-MXR) in an undoped YAG crystal. Continuous radiation at 1.92 eV for the comparison study was provided by a solid-state laser.

For the 3.06 eV excitation, we computed the applied laser fluence on the sample using the measured spot diameter of 1.4 μm produced by a ×40 microscope objective. Taking into account the influence of the substrate and the dielectric function of the $WSe_2$ monolayer[39], we find that the absorbed fluence is 2.2% of the applied fluence. An upper bound for the exciton density is obtained by assuming full conversion of the absorbed photons into excitons. This is probably an overestimate of the true exciton density, as recent reports indicate incomplete relaxation of carriers produced at higher photon energies to band-edge excitons[40]. The pump laser radiation, in addition to producing excitons, can potentially change the nature of the sample by altering the charge density (through photodoping) or the temperature (through heating effects). Although some photodoping was observed, the degree of photodoping was essentially independent of laser fluence (Supplementary Information). Hence, this process does not influence the measured fluence-dependent properties. Similarly, equilibrium heating was shown to be negligible based on the lack of spectral shifts (see Supplementary Information).

We measured the emitted PL in a back-scattering configuration with a grating spectrometer and a liquid-nitrogen cooled CCD for spectroscopic analysis. As an alternative, we detected the PL with a fast avalanche photodiode (PicoQuant PDM) and analysed the temporal profile of the emission by time-resolved single photon counting (PicoQuant PicoHarp 300). We determined the instrument response function (IRF) of the TR-PL set-up using 1.53 eV fs pulses from the Ti:sapphire laser. In comparing models with the experimental time traces, we convolved the predicted form with the measured IRF.

**Theoretical.** Within the rate-equation model of the dynamics, the cross-section $\sigma$ for biexciton formation is estimated from the parameter $\beta$ in equation (1) using the kinetic theory relation $\beta = \sigma v_{rel}$, where $v_{rel}$ is the relative exciton velocity. Assuming a 2D Maxwellian velocity distribution at 10 K for excitons of mass $0.68m_e$ (refs 3,30), we infer a biexciton formation cross-section of $\sigma \approx 4$ nm. As the actual exciton velocity distribution may exceed that implied by the base temperature of the sample (because of hot carrier effects), this analysis may overestimate the formation cross-section. Still, the inferred value is comparable to the exciton Bohr radius of ∼1 nm (ref. 30).

We examined the biexciton states in $WSe_2$ monolayers theoretically using a variational calculation within an effective mass approximation to describe carriers at the K/K′ band edge (see Supplementary Information). Although the general scheme is similar to that applied in previous studies of quantum wells, a critical difference is the form of the Coulomb interaction between charges. Because of the atomic-level thickness of the material, the dielectric screening is non-local in character. We model the interaction using the electrostatic interaction for charges in a 2D dielectric sheet. The e–h potential in reciprocal space is then given by[30,35] $V(q) = -2\pi e^2/q(1 + r_0 q)$, where $r_0$ is a screening length, which is proportional to the 2D polarizability of the sheet. For the $WSe_2$ monolayer, we use $r_0 = 45$ Å and electron and hole mass parameters of $m_e = m_h = 0.34m_0$, where $m_0$ denotes the free electron mass[3,30]. The variational wavefunction, which includes six variational parameters, allows interpolation of the biexciton configuration from equal sharing of charges to two completely separated excitons, as well as inclusion of the correlation between like charges. Both pairs of electrons and holes are assumed to be in singlet states. (See Supplementary Section 8, for details concerning the calculation.)

## References

39. Li, Y. *et al.* Measurement of the optical dielectric function of monolayer transition-metal dichalcogenides: $MoS_2$, $MoSe_2$, $WS_2$, and $WSe_2$. *Phys. Rev. B* **90,** 205422 (2014).
40. Kozawa, D. *et al.* Photocarrier relaxation pathway in two-dimensional semiconducting transition metal dichalcogenides. *Nature Commun.* **5,** 4543 (2014).

nature COMMUNICATIONS

ARTICLE

DOI: 10.1038/s41467-018-05917-8 OPEN

# Efficient generation of neutral and charged biexcitons in encapsulated $WSe_2$ monolayers

Ziliang Ye[1,2], Lutz Waldecker[1], Eric Yue Ma[1], Daniel Rhodes[3], Abhinandan Antony[3], Bumho Kim[3], Xiao-Xiao Zhang[1], Minda Deng[1], Yuxuan Jiang[4], Zhengguang Lu[4,5], Dmitry Smirnov[4], Kenji Watanabe[6], Takashi Taniguchi[6], James Hone[3] & Tony F. Heinz[1,7]

Higher-order correlated excitonic states arise from the mutual interactions of excitons, which generally requires a significant exciton density and therefore high excitation levels. Here, we report the emergence of two biexcitons species, one neutral and one charged, in monolayer tungsten diselenide under moderate continuous-wave excitation. The efficient formation of biexcitons is facilitated by the long lifetime of the dark exciton state associated with a spin-forbidden transition, as well as improved sample quality from encapsulation between hexagonal boron nitride layers. From studies of the polarization and magnetic field dependence of the neutral biexciton, we conclude that this species is composed of a bright and a dark excitons residing in opposite valleys in momentum space. Our observations demonstrate that the distinctive features associated with biexciton states can be accessed at low light intensities and excitation densities.

[1] Department of Applied Physics, Stanford University, 348 Via Pueblo Mall, Stanford, CA 94305, USA. [2] Department of Physics and Astronomy, University of British Columbia, Vancouver, BC V6T 1Z4, Canada. [3] Department of Mechanical Engineering, Columbia University, New York, NY 10027, USA. [4] National High Magnetic Field Laboratory, Tallahassee, FL 32310, USA. [5] Department of Physics, Florida State University, Tallahassee, FL 32306, USA. [6] National Institute for Materials Science, 1-1 Namiki, Tsukuba 305-0044, Japan. [7] SLAC National Accelerator Laboratory, Menlo Park, CA 94025, USA. Correspondence and requests for materials should be addressed to T.F.H. (email: tony.heinz@stanford.edu)

The strong Coulomb interaction in two-dimensional transition metal dichalcogenide (TMDCs) crystals, arising from reduced dielectric screening in the atomically thin limit, significantly modifies the optical properties of these materials and gives rise to pronounced excitonic effects[1]. The Coulomb attraction between electrons and holes in these systems leads to the formation of tightly bound excitons, which causes a reduction in the optical band gap by a large fraction of an electron volt and yields very short intrinsic radiative lifetimes[2–5]. Both trion (charged exciton) and biexciton (exciton molecule) states have been observed in TMDCs[6–8]. Here we report on the characterization of a second biexciton species in monolayer $WSe_2$, in addition to the previously observed species[7], which we identify as the neutral and negatively charged biexciton (four-particle and five-particle) states, respectively. In our high-quality samples produced using encapsulation in hexagonal boron nitride (hBN), local inhomogeneities and nonradiative decay channels in the monolayer semiconductor are strongly reduced. As a consequence, the emission of the neutral and charged biexciton is observed at an excitation density three orders of magnitude lower than in previous reports. By comparing the emission of the different exciton species under strong magnetic fields and as a function of doping level, we deduce that the neutral biexciton is formed predominantly from the combination of a dark (spin-forbidden) and bright (spin-allowed) exciton residing in opposite valleys in momentum space. Our observations provide new understanding of many-body excited states in 2D semiconductors and open a path for utilizing the features of biexcition states for quantum and optoelectronic applications at low light intensities.

The lowest lying interband transition in monolayer tungsten compounds of the TMDC family has been identified as spin-forbidden[9]. The exciton associated with the lower conduction band therefore, to first order, does not emit light; it is referred to as a dark exciton. The existence of dark excitons strongly influences the optical properties of the material, including the photoluminescence (PL) quantum efficiency at low temperatures[10], the ultranarrow linewidth of the PL emission along the in-plane direction[11], the efficient coupling to surface plasmon polaritons[12], and the large tip-induced enhancement of the PL[13]. Because the dark exciton has a lifetime that is orders of magnitude longer than the bright exciton at low temperature[14], the steady-state density of dark excitons can be much higher than that of bright excitons for continuous-wave excitation. Correspondingly, the diffusion length of the dark exciton is also enhanced. When a dark exciton approaches another exciton, the two excitons can interact to form a biexciton (Fig. 1a). Therefore, the formation of biexcitons via the long-lived dark exciton states is much more likely than through two short-lived bright excitons. Here we report the observation of a neutral and charged biexciton composed of both bright and dark excitons.

## Results

**Observation of biexcitons in the charge-neutral regime**. We observe the evidence of a biexciton in our high-quality encapsulated $WSe_2$ samples (see Methods). In these samples, the defect density of the TMDC is reduced by about two orders of magnitude ($5 \times 10^{10}\,cm^{-2}$) by exfoliating flux-grown crystals. The observed bright exciton linewidth (FWHM 4.5 meV at 20 K) is approaching the radiative limit[15]. In the low-temperature PL spectrum, the spin-allowed bright exciton emission appears at 1.723 eV (Fig. 1c). Emission from the spin-forbidden dark exciton with a linewidth of only 0.8 meV and an out-of-plane dipole radiation pattern (Supplementary Fig. 1) is observed at 1.681 eV, in agreement with previous reports[11,12]. As the excitation power is increased, a new peak emerges at 1.703 eV, lying 20 meV below the bright exciton peak. Compared to the emission of the bright and dark exciton species, which rise nearly linearly with laser intensity, the new peak increases approximately quadratically. A power-law fit of the emission yields an exponent of $1.96 \pm 0.03$ (Fig. 1d). The quadratic intensity dependence suggests that the peak arises from a few-body state formed from two excitons, each exhibiting a concentration growing linearly with intensity (Supplementary Note 2). The new biexciton peak, we should note, is observed for rather weak continuous wave (cw) excitation, with an irradiance of $1.4 \times 10^3\,W/cm^2$, more than three orders of magnitude lower than in typical experiments employing pulsed laser excitation[7]. The asymmetric peak $X^i$, lying 32 meV below $X^0$, and the series of peaks around 1.665 eV have been attributed to indirect (momentum-dark) excitons[16]. The lower-lying emission peaks also originate from the $WSe_2$ sample, but have an unknown origin and are beyond the scope of this work.

**Spin and valley configuration of the biexciton**. In the following, we focus on identifying the composition of the newly observed biexciton state. Regarding the spin degree of freedom, biexcitons can be classified as composed of dark–dark, dark–bright, and bright–bright exciton components. (Here we assume the electron and hole of the constituent excitons remain in the same band when forming a biexciton.) The emission energy of the biexciton precludes it from being composed of two dark excitons, as this would require a negative binding energy. The bright–bright configuration is unlikely to occur given our experimental conditions: At the greatest applied laser intensity, we estimate an upper limit of $52\,\mu m^{-2}$ of bright excitons in the steady state, for a 2-ps lifetime of the bright exciton[5] and assuming a 100% conversion efficiency from absorbed photons to bright excitons. This density is smaller than the dark exciton density at our lowest excitation level, as the dark exciton has a lifetime more than 50 times longer than the bright species, as reported by Robert et al.[14] and confirmed in our sample. The low density of bright excitons renders the bright–bright biexciton much less likely to form. (A simple kinetic model is presented in Supplementary Note 3 to describe the biexciton formation process.) We therefore conclude that the observed biexciton is a combination of one bright and one dark exciton (Fig. 1b). This assignment is further supported by the magnetic field and doping dependences of the biexciton emission, as discussed below.

To investigate the biexciton valley configuration further, we apply a strong out-of-plane magnetic field, which acts to break the valley degeneracy. As a magnetic field along the normal direction of the sample shifts the conduction and valence bands in the different valleys in opposite directions, the exciton peaks are split into pairs[17–19] associated with their valley index. Since the dark exciton has a total spin angular momentum of 1, its Zeeman splitting is larger than that of the bright exciton[14] with its vanishing total spin. As the emission of the biexciton results from its bright component, leaving behind a dark exciton in the final state, the biexciton emission energy is given by the bright exciton emission energy reduced by the biexciton binding energy $\Delta_{XX}$ (see Methods). Neglecting any difference in magnetic field dependence of the (small) biexciton binding energy $\Delta_{XX}$, we predict within our picture that the XX peak should exhibit the same $g$-factor as the bright exciton. This agrees with our experimental observations: $X^0$ and XX have $g$-factors of $4.4 \pm 0.5$ and $4.6 \pm 0.5$, respectively, while $X^D$ has a $g$-factor of $9.6 \pm 0.5$ (Fig. 2a).

The distribution of the exciton population between the different branches of the Zeeman-split pairs will, in thermal equilibrium, follow a Boltzmann distribution. This suggests that

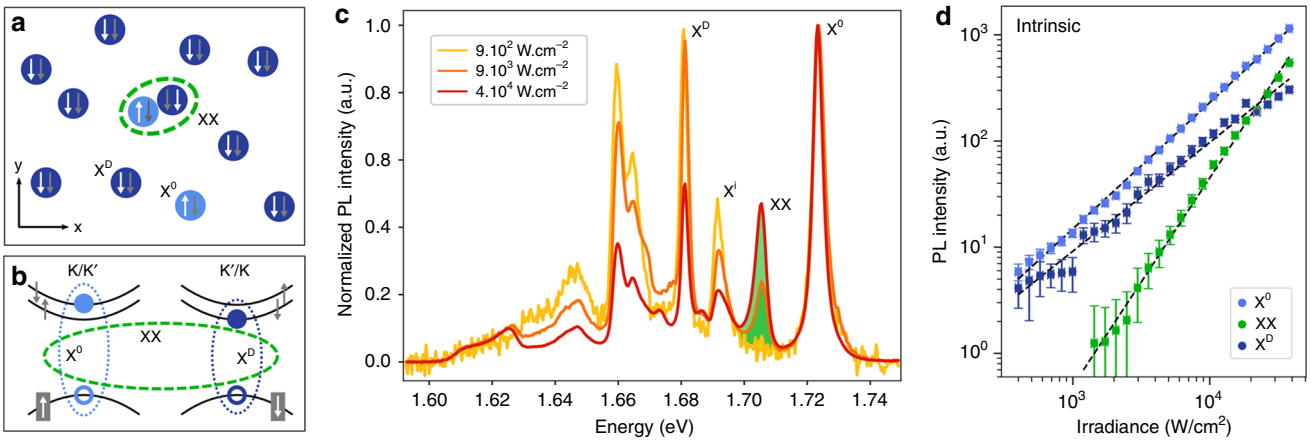


**Fig. 1** Observation of a biexciton composed of a bright (spin-allowed) and a dark (spin-forbidden) exciton. **a** Schematic of biexciton formation in real space. Because the dark exciton ($X^D$, dark blue) has a total spin of 1, it has a much longer radiative lifetime and therefore a much higher density than the bright exciton ($X^0$, light blue), which has a total spin of zero. A biexciton (XX, green circle) can form as a bright and a dark exciton approach one another. **b** Representation of the biexciton in momentum space. **c** Photoluminescence (PL) spectra of an encapsulated $WSe_2$ monolayer sample for different excitation intensities. All spectra are normalized to the $X^0$ peak. A new peak (green shading) emerges at high excitation levels and is attributed to biexciton emission. The XX peak is located at 1.703 eV, 20 meV below the $X^0$ peak. The $X^D$ peak at 1.681 eV is identified by examining its distinct radiation pattern. Other peaks are discussed in the main text. **d** Power dependence of the emission of different excitonic species. Datapoints and errorbars are results of pseudoVoigt fits to the raw spectra. The XX peak grows superlinearly with incident intensity with an exponent of 1.96. In contrast, the $X^0$ and $X^D$ peaks have exponents of 1.22 and 1.03, respectively

even for a partially thermalized system, which starts from equal populations when degenerate, the low-energy branch (LEB) of the pair should have a larger population, and thus emit more light, than the high-energy branch (HEB). This relation is satisfied for the pairs of dark excitons and most of the features seen in the PL. However, for the bright exciton pair, the emission intensity is comparable, and in some conditions inverted. Such an unusual distribution might arise from the efficient intervalley scattering between two conduction bands of same spin (see Supplementary Note 4 for a detailed discussion). More importantly, the emission intensity from the biexciton pair is also observed to be inverted, with an inversion even more pronounced than for the bright exciton. This observation suggests the biexciton to be composed of a bright and a dark exciton residing in opposite valleys. In the intervalley configuration (Fig. 2c), the dark component in the HEB (LEB) of the biexciton is associated with the LEB (HEB) of the dark exciton[17]. We expect that the rate of biexciton formation should scale as the product of the constituent exciton densities, that is $\propto \rho_{X^D,L(H)} \cdot \rho_{X^0,H(L)}$. If the density of biexcitons $\rho_{XX,H(L)}$ is much smaller than that of bright excitons, after being normalized to their lifetimes, the biexciton density will scale in the same fashion (see Supplementary Note 2). With the experimentally observed larger population of the dark exciton in the LEB, an intervalley configuration of the biexciton leads naturally to an inverted distribution for the biexciton emission. More quantitatively, the LEB/HEB ratio of the biexciton pair should be close to the quotient of the ratios observed in the bright and dark exciton pairs, a result consistent with our experimental findings at different magnetic fields (Fig. 2b).

The fact that the intervalley configuration of the biexciton is favored over other configurations can be understood in terms of energetics. The intravalley configuration—bright and dark excitons residing in the same valley—needs to involve two holes sharing the same valence band, which costs extra energy as Pauli blocking forces the second hole to occupy a higher momentum/energy state (the footprint of an exciton in momentum space can be approximated by the inverse of the exciton Bohr radius of about 1 nm). Another possible configuration would be that of a biexciton composed of a direct and an indirect exciton—two electrons are located in different bands of the same valley, but with the two holes in opposite valleys. This configuration costs extra exchange energy, which should be about 10 meV as inferred from the peak separation between the two negatively charged trions[20,21]. Within our experiment, we cannot, however, exclude potential contributions from Q point indirect excitons[22].

**Distinguishing neutral and negatively charged biexcitons.** Finally, we are able to elucidate the relationship between the newly observed and the previously reported biexciton[7] by tuning the static carrier density in the material (Fig. 3a). In the low excitation regime, the emission spectra agree well with those reported in the literature: the bright and dark excitons are observed in the intrinsic regime while different types of trions emerge in the n-doped and p-doped regimes[20,21]. Unlike the bright exciton state, which extends to finite doping levels with an asymmetric gate dependence, the dark exciton is strictly limited to the intrinsic regime. Under stronger excitation conditions ($\sim 4 \times 10^3$ W cm$^{-2}$), the biexciton peak at 1.703 eV appears, and its emission is also restricted to the intrinsic regime. The doping dependence therefore confirms that this newly observed XX peak results from a neutral biexciton formed by a bright and a dark exciton, as it appears only in the doping regime where both types of excitons coexist (Fig. 3b).

Under strong excitation conditions, the emission of another biexciton is observed in our spectra, which exhibits a superlinear power dependence with an emission strength scaling with the pump laser intensity as $I^{1.56}$ (Supplementary Fig. 2). This peak lies 52 meV below the bright exciton and has been reported in the literature[7]. However, this biexciton only appears at the crossover from the intrinsic to the n-doped regime (Fig. 3b), suggesting that it is a negatively charged biexciton $XX^-$, formed from a trion and a neutral exciton, as opposed to its earlier assignment as a neutral biexciton[7]. In contrast to the negatively charged trions, no fine

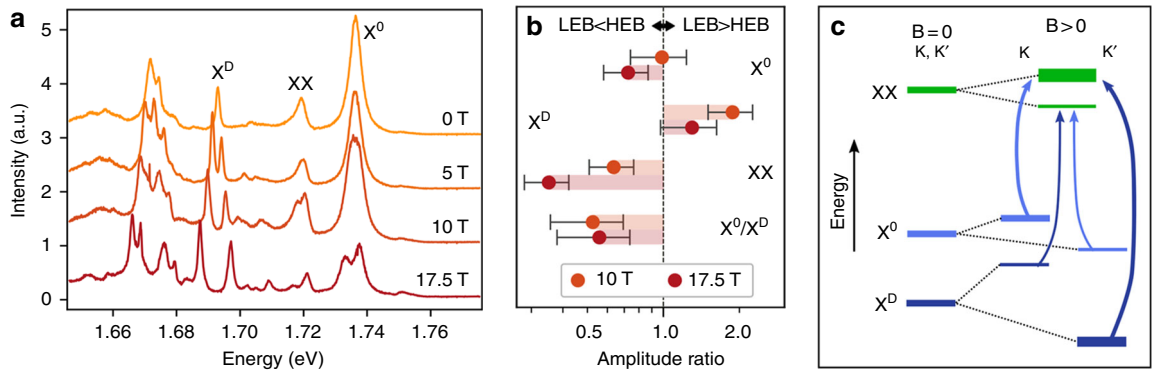


**Fig. 2** Zeeman splitting and non-equilibrium distribution of biexciton emission. **a** A strong out-of-plane magnetic field splits most emission peaks into pairs. The splitting of XX is similar to that of the $X^0$ feature (*g*-factor 4.4 ± 0.5), whereas the splitting of the $X^D$ feature is larger because of its non-zero spin. **b** The ratios of amplitudes of the fitted low-energy branch (LEB) and high-energy branch (HEB) of the emission spectra. Unlike the $X^D$ pair, the XX emission pair exhibits inverted populations between the HEB and LEB. The LEB/HEB ratio of the XX pair is similar to that of $X^0/X^D$. The error bars for $X^0$, $X^D$, and XX are conservative estimates. **c** A diagram of the biexciton intervalley configuration as probed through the PL measurements in a magnetic field. The B-field splits the bright (light blue) and dark (dark blue) exciton into pairs according to their valley index (*K*, *K′*). Analysis of the PL intensities shows that the biexciton is composed of excitons from different valleys

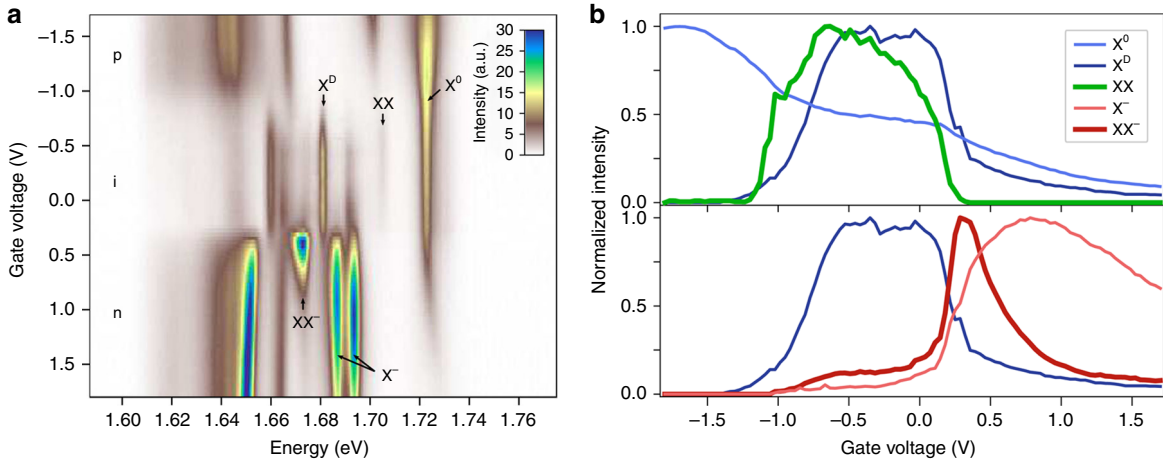


**Fig. 3** Doping dependence of the PL emission of neutral and charged biexcitons. **a** Gate dependence map of the PL intensity above the onset for observing both biexciton species ($I_0 = 4 \times 10^3$ W cm$^{-2}$). The intrinsic regime is characterized by the strong emission from $X^D$. In the n-doped and p-doped regimes, trions and other species emerge. The XX peak at 1.703 eV is only observed in the intrinsic regime, indicating a neutral biexciton composed of a neutral $X^0$ and $X^D$. Another peak with superlinear power dependence is observed at 1.671 eV, 52 meV below $X^0$. It is assigned to a charged biexciton state, as it appears only in the low n-doped regime. **b** Normalized PL intensity of the exciton species relevant for the formation of biexcitons as a function of doping level. The neutral biexciton (green) emission is limited to the intrinsic regime, in which $X^D$ (dark blue) is observed, showing the important role of $X^D$ in the formation of XX. The $XX^-$ emission (dark red) is strongest in the low n-doped regime, where $X^0$ (light blue), $X^D$ and the two $X^-$ species coexist (light red, only lower $X^-$ shown for clarity)

features can be resolved in the $XX^-$ peak at this stage. If no more than one electron/hole resides in any band, there should be two spin-valley configurations for $XX^-$. Due to the conduction band splitting, we expect the energetically favored configuration to be two holes in opposite valence band valleys, two electrons in opposite lower conduction band valleys and one electron in the higher conduction band. Because the valence band splitting is much larger —about 400 meV—no positively charged biexciton ($XX^+$) emission would be observed. Since the $XX^-$ peak appears most prominently at relatively low doping levels, we can rule out the possibility of it being related to a plasmon coupled exciton[23]. With respect to the two negatively charged trions, the $XX^-$ has a binding energy of 14 or 21 meV, in agreement with theoretical calculations[24].

## Discussion

The identification of neutral and charged biexcitons resolves the discrepancy of the biexciton binding energy found between previous experiments and theories: as calculated, the biexciton binding energy is indeed smaller than the trion binding energy due to the form of the screened Coulomb potential in two-dimensional TMDCs[24–28]. The 20-meV binding energy also matches that of the neutral biexciton in $MoSe_2$ monolayers observed by Hao et al. using two-dimensional coherent spectroscopy[8] and of $WSe_2$ in pump-probe spectroscopy[29], even though both works describe bright–bright excitons, which would suggest the biexciton binding energy is only weakly sensitive to the spin configuration of the two constituent excitons.

In conclusion, we have observed neutral and charged biexciton species in monolayer $WSe_2$ crystals encapsulated in hBN through their clear emission signatures. We have established that the neutral biexciton is composed of pairs of excitons located in opposite valleys, one of which is a long-lived dark species. Our observations deepen the understanding of the intrinsic optical properties of two-dimensional TMDCs and provides a new route to access the optical response associated with biexciton species under conditions of modest excitation.

## Methods

**Samples**. Single crystals were grown by sealing W powder, 99.999% purity, and Se shot, 99.999% purity, in an evacuated quartz ampoule with excess Se as the flux. Subsequently, the ampoule was heated to 1000 °C for 2 days and cooled to 450 °C at a rate of 0.85 °C $h^{-1}$. The crystals were removed, centrifuged, and annealed at 250 °C for 2 days to remove excess Se. Encapsulated monolayers of $WSe_2$ were then prepared from these single crystals by a dry stamping technique[30], with all materials exfoliated on $Si/SiO_2$ substrates. In order to contact the $WSe_2$ film, two few-layer graphene strips were picked up by an hBN flake, followed by the monolayer $WSe_2$. Finally, a bottom ($Ar/O_2$ cleaned) hBN crystal and a thin layer of graphite were picked up to act as the backgate for controlling doping and screening the effects of the $SiO_2$. Contact was made to the graphite leads and backgate by etching with $CHF_3$ and making edge contact using Cr/Pd/Au film deposition (2/25/50 nm).

**Measurements**. In all but the magnetic field experiments, the samples were mounted in a continuous flow optical cryostat and cooled with liquid helium to temperatures of ~15 K. PL spectra were taken with an imaging spectrometer after 640 nm cw laser excitation. We note that for laser excitation at shorter wavelengths (e.g., 532 nm), we observed photodoping of the sample starting at moderate power levels. Spectra on bare hBN were taken to verify that all features in Fig. 1b originate from the $WSe_2$ sample. Magnetic field measurements were conducted at the National High Magnetic Field Laboratory, at sample temperatures of 10 K and cw laser excitation at 660 nm. The PL spectra were fitted with a series of pseudoVoigt lineshapes to obtain the emission intensity (area) as a function of the relevant experimental parameters.

**Biexciton binding energy**. The binding energy Δ of the neutral biexciton is obtained from the relation for energy conservation in the formation and radiative decay of the biexciton species: $E_{X^0} + E_{X^0} - \Delta = \hbar\omega_{XX} + E_{X^D}$. Here we consider a biexciton formed from a pair of bright and dark excitons and assume that the final state after radiative decay is a dark exciton in its ground state. It follows that the biexciton binding energy is directly related to experimentally observable emission energies through $\Delta = E_{X^0} - \hbar\omega_{XX}$.

## Data availability

The data supporting the plots within this paper and other findings of this study are available from the corresponding author upon request.

Received: 14 March 2018 Accepted: 28 July 2018
Published online: 13 September 2018

## References

1. Wang, G. et al. Excitons in atomically thin transition metal dichalcogenides. *Rev. Mod. Phys.* **90**, 21001 (2018).
2. He, K. et al. Tightly bound excitons in monolayer $WSe_2$. *Phys. Rev. Lett.* **113**, 026803 (2014).
3. Ye, Z. et al. Probing excitonic dark states in single-layer tungsten disulfide. *Nature* **513**, 214–218 (2014).
4. Chernikov, A. et al. Exciton binding energy and nonhydrogenic rydberg series in monolayer $WS_2$. *Phys. Rev. Lett.* **113**, 076802 (2014).
5. Robert, C. et al. Exciton radiative lifetime in transition metal dichalcogenide monolayers. *Phys. Rev. B* **93**, 205423 (2016).
6. Mak, K. F., He, K., Shan, J. & Heinz, T. F. Control of valley polarization in monolayer $MoS_2$ by optical helicity. *Nat. Nanotechnol.* **7**, 494–498 (2012).
7. You, Y. et al. Observation of biexcitons in monolayer $WSe_2$. *Nat. Phys.* **11**, 477–482 (2015).
8. Hao, K. et al. Neutral and charged inter-valley biexcitons in monolayer $MoSe_2$. *Nat. Commun.* **8**, 15552 (2017).
9. Zhang, X. X. et al. Magnetic brightening and control of dark excitons in monolayer $WSe_2$. *Nat. Nanotechnol.* **12**, 883–888 (2017).
10. Zhang, X.-X., You, Y., Zhao, S. Y. F. & Heinz, T. F. Experimental evidence for dark excitons in monolayer $WSe_2$. *Phys. Rev. Lett.* **115**, 257403 (2015).
11. Wang, G. et al. In-plane propagation of light in transition metal dichalcogenide monolayers: optical selection rules. *Phys. Rev. Lett.* **119**, 047401 (2017).
12. Zhou, Y. et al. Probing dark excitons in atomically thin semiconductors via near-field coupling to surface plasmon polaritons. *Nat. Nanotechnol.* **12**, 856–860 (2017).
13. Park, K. D., Jiang, T., Clark, G., Xu, X. & Raschke, M. B. Radiative control of dark excitons at room temperature by nano-optical antenna-tip Purcell effect. *Nat. Nanotechnol.* **13**, 59–64 (2018).
14. Robert, C. et al. Fine structure and lifetime of dark excitons in transition metal dichalcogenide monolayers. *Phys. Rev. B* **96**, 155423 (2017).
15. Ajayi, O. A. et al. Approaching the intrinsic photoluminescence linewidth in transition metal dichalcogenide monolayers. *2D Mater.* **4**, 031011 (2017).
16. Lindlau, J. et al. Identifying optical signatures of momentum-dark excitons in transition metal dichalcogenide monolayers. Preprint at http://arxiv.org/abs/1710.00988 (2017).
17. Aivazian, G. et al. Magnetic control of valley pseudospin in monolayer $WSe_2$. *Nat. Phys.* **11**, 148–152 (2015).
18. Li, Y. et al. Valley splitting and polarization by the zeeman effect in monolayer $MoSe_2$. *Phys. Rev. Lett.* **113**, 266804 (2014).
19. Macneill, D. et al. Breaking of valley degeneracy by magnetic field in monolayer $MoSe_2$. *Phys. Rev. Lett.* **114**, 037401 (2015).
20. Plechinger, G. et al. Trion fine structure and coupled spin-valley dynamics in monolayer tungsten disulfide. *Nat. Commun.* **7**, 12715 (2016).
21. Courtade, E. et al. Charged excitons in monolayer $WSe_2$: experiment and theory. *Phys. Rev. B* **96**, 085302 (2017).
22. Zhang, C. et al. Probing critical point energies of transition metal dichalcogenides: surprising indirect gap of single layer $WSe_2$. *Nano Lett.* **15**, 6494–6500 (2015).
23. Van Tuan, D., Scharf, B., Zutić, I. & Dery, H. Marrying excitons and plasmons in monolayer transition-metal dichalcogenides. *Phys. Rev. X* **7**, 041040 (2017).
24. Kylänpää, I. & Komsa, H. P. Binding energies of exciton complexes in transition metal dichalcogenide monolayers and effect of dielectric environment. *Phys. Rev. B* **92**, 205418 (2015).
25. Zhang, D. K., Kidd, D. W. & Varga, K. Excited biexcitons in transition metal dichalcogenides. *Nano Lett.* **15**, 7002–7005 (2015).
26. Mayers, M. Z., Berkelbach, T. C., Hybertsen, M. S. & Reichman, D. R. Binding energies and spatial structures of small carrier complexes in monolayer transition-metal dichalcogenides via diffusion Monte Carlo. *Phys. Rev. B* **92**, 161404(R) (2015).
27. Kidd, D. W., Zhang, D. K. & Varga, K. Binding energies and structures of two-dimensional excitonic complexes in transition metal dichalcogenides. *Phys. Rev. B* **93**, 125423 (2016).
28. Szyniszewski, M., Mostaani, E., Drummond, N. D. & Fal'ko, V. I. Binding energies of trions and biexcitons in two-dimensional semiconductors from diffusion quantum Monte Carlo calculations. *Phys. Rev. B* **95**, 081301(R) (2017).
29. Steinhoff, A. et al. Biexciton fine structure in monolayer transition metal dichalcogenides. Preprint at http://arxiv.org/abs/1801.04225 (2018).
30. Castellanos-Gomez, A. et al. Deterministic transfer of two-dimensional materials by all-dry viscoelastic stamping. *2D Mater.* **1**, 011002 (2014).

## Acknowledgements

The authors thank Timothy Berkelbach and Ting Cao for fruitful discussions. The spectroscopic studies were supported by the Department of Energy, Office of Science, Basic Energy Sciences, Materials Sciences and Engineering Division, under Contract DE-AC02-76SF00515 for the magnetic field measurements and by the Gordon and Betty Moore Foundation's EPiQS Initiative through Grant no. GBMF4545 for analysis. Sample preparation was supported by the National Science Foundation MRSEC program through Columbia in the Center for Precision Assembly of Superstratic and Superatomic Solids (DMR-1420634). L.W. acknowledges support by the Alexander von Humboldt Foundation. Y.J., Z.L. and D.S. acknowledge support from the US Department of Energy (DE-FG02-07ER46451) for magneto-photoluminescence measurements performed at the National High Magnetic Field Laboratory, which is supported by the NSF Cooperative Agreement no. DMR-1157490 and the State of Florida.

## Author contributions

Z.Y., L.W. and T.F.H. conceived the project. D.R., A.A. and B.K. grew the $WSe_2$ crystals and prepared encapsulated and backgated samples. K.W. and T.T. produced the hBN crystals. Z.Y., L.W., E.Y.M., Y.J., X.Z. and M.D. conducted the measurements. Z.Y. and

L.W. analyzed the data. Z.Y., L.W. and T.F.H. wrote the manuscript with input from all authors.

## Additional information

**Supplementary Information** accompanies this paper at https://doi.org/10.1038/s41467-018-05917-8.

**Competing interests:** The authors declare no competing interests.

**Reprints and permission** information is available online at http://npg.nature.com/reprintsandpermissions/

**Publisher's note:** Springer Nature remains neutral with regard to jurisdictional claims in published maps and institutional affiliations.